# Predictive Cost Adaptive Control of In-Ground-Effect Flight using Active Flow Control with Unmodeled, Unsteady Aerodynamics

Jacob C. Vander Schaaf*, Qizhi Lu†, Harsh Kumar‡, Baris Ozmadenci§,
Krzysztof J. Fidkowski¶, and Dennis S. Bernstein‖
*University of Michigan, Ann Arbor, Michigan, 48109*

**In-ground-effect (IGE) flight offers significant advantages in terms of fuel efficiency and stealth. This paper investigates the feasibility of IGE flight using predictive cost adaptive control (PCAC). As an indirect adaptive control extension of model predictive control, PCAC uses recursive least squares with variable-rate forgetting for online, closed-loop system identification. For 2D IGE flight of an airfoil over a sinusoidal wave surface, PCAC uses active flow control with either jet actuation or trailing-edge flap deflection to suppress the effect of unsteady aerodynamics without the need for a prior control-oriented model.**

## I. Introduction

In-ground-effect (IGE) flight offers significant advantages in terms of fuel efficiency, and thus range and payload, as well as stealth. This paper investigates the feasibility of IGE flight over varied seas with unmodeled, unsteady aerodynamics [1]. The approach taken in this paper is based on predictive cost adaptive control (PCAC). As an indirect adaptive control extension of model predictive control (MPC), PCAC uses recursive least squares (RLS) with variable-rate forgetting (VRF) for online, closed-loop system identification [2–6]. At each time step, RLS-based system identification updates the coefficients of an input-output model whose order is specified by the user. To determine control inputs, PCAC uses quadratic programming for receding horizon optimization, which enforces magnitude- and rate-saturation constraints as well as output constraints. To enable output-feedback control, PCAC uses the block-observable canonical form (BOCF) realization, which provides exact state estimation at every step [7].

PCAC can be used with a reference model, and unknown disturbances may be either matched or unmatched. During operation, PCAC uses sampled sensor data (e.g., flow state and altitude) and requests system inputs (e.g., surface deflections and fluidic-jet velocities). Other than specification of the model order, optimization horizon, and forgetting parameters, PCAC operates under cold-start conditions without the need for any prior control-oriented model.

PCAC represents a radical departure from conventional autopilot synthesis. In particular, autopilots for fixed-wing aircraft are typically designed based on linearized aerodynamic models consisting of stability and control derivatives obtained from wind-tunnel testing. The resulting local controllers are then pieced together using gain scheduling. PCAC eliminates the need for this approach, which is laborious and requires considerable expertise.

The actuation methods used in the present paper for IGE flight are a fluidic jet and a trailing-edge flap deflection. These actuation mechanisms interact directly with the flow field around the airfoil, thus constituting active flow control strategies. Standard techniques for active flow control typically depend on detailed modeling of the fluid dynamics, either analytically or experimentally, often followed by model reduction [8–18]. Controller-synthesis techniques used for flow control include optimal control [19, 20], robust control [21], and machine-learning methods [17, 22]. In contrast, PCAC relies entirely on a model that is identified online, and thus requires no reduced-order model of any kind, either extracted from offline data or a high-order analytical model.

The online, closed-loop system identification based on RLS/VRF used by PCAC provides a linear model, which facilitates the receding-horizon optimization. The high Reynolds number fluid dynamics of IGE flight are highly nonlinear, and thus the efficacy of a linear model identified online must be assessed through numerical studies, as in the present paper.

The present paper focuses on 2D IGE flight of an airfoil over a sinusoidal wave surface. Two types of control actuation are considered, namely, trailing-edge flap deflection and fluidic-jet velocity modulation. Using both types

*Ph.D. Candidate, Department of Aerospace Engineering, jacobcvs@umich.edu.
†Master's Student, Department of Aerospace Engineering, luqseven@umich.edu.
‡Master's Student, Department of Aerospace Engineering, kharsh@umich.edu.
§Master's Student, Department of Aerospace Engineering, barisoz@umich.edu.
¶Professor, Department of Aerospace Engineering, kfid@umich.edu.
‖Professor, Department of Aerospace Engineering, dsbaero@umich.edu.

of actuation, PCAC is shown to suppress the effect of unsteady aerodynamics with no prior model available to the controller. The CFD simulations are implemented in ANSYS Fluent for the fluidic-jet velocity modulation and in xflow for the trailing-edge flap deflection. xflow is a high-order, mesh-adaptive CFD [23, 24], which is efficient for obtaining high-accuracy results for practical aerodynamic simulations.

## II. Review of Predictive Cost Adaptive Control

As shown in Figure 1, predictive cost adaptive control (PCAC) combines online identification with output-feedback model predictive control (MPC). PCAC uses no a priori modeling information aside from a suitable model order for system identification, nor does it use probing signals.

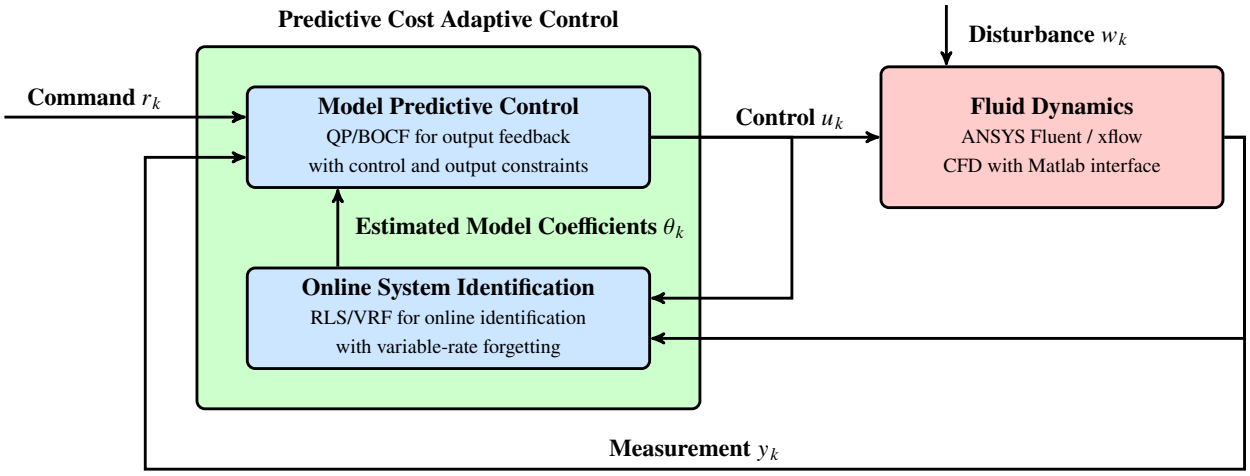


**Fig. 1 PCAC block diagram. The online, closed-loop system identification is based on recursive least squares (RLS) with variable-rate forgetting (VRF). The model predictive control (MPC) algorithm, which is based on quadratic programming (QP), uses the estimated model coefficients $\theta_k$ to form a block-observable canonical form (BOCF) state-space model, which is used by QP to determine the control input $u_k$.**

### A. Online Identification

To perform online, closed-loop system identification, we first consider the MIMO input-output model

$$\hat{y}_k = -\sum_{i=1}^{\hat{n}} \hat{F}_i y_{k-i} + \sum_{i=1}^{\hat{n}} \hat{G}_i u_{k-i}, \tag{1}$$

where $k \geq 0$ is the step, $\hat{n} \geq 1$ is the identification data window, $\hat{F}_i \in \mathbb{R}^{p\times p}$ and $\hat{G}_i \in \mathbb{R}^{p\times m}$ are the estimated model coefficients, and $u_k \in \mathbb{R}^m$, $y_k \in \mathbb{R}^p$, and $\hat{y}_k \in \mathbb{R}^p$ are the inputs, outputs, and predicted outputs. We estimate $\hat{F}_k$ and $\hat{G}_k$ online using recursive least squares with variable-rate forgetting (RLS/VRF), by minimizing the cost function [3]

$$J_k(\hat{\theta}) = \sum_{i=0}^{k} \frac{\rho_i}{\rho_k} z_i^{\mathrm{T}}(\hat{\theta}) z_i(\hat{\theta}) + \frac{1}{\rho_k}(\hat{\theta} - \theta_0)^{\mathrm{T}} P_0^{-1} (\hat{\theta} - \theta_0), \tag{2}$$

where $\rho_k \triangleq \prod_{j=0}^{k} \lambda_j^{-1} \in \mathbb{R}$, $\lambda_k \in (0, 1]$ is the forgetting factor, $P_0 \in \mathbb{R}^{[\hat{n}p(m+p)]\times[\hat{n}p(m+p)]}$ is positive definite, $\theta_0 \in \mathbb{R}^{[\hat{n}p(m+p)]}$ is the initial estimate of the coefficient vector, and the performance variable $z_i(\hat{\theta}) \in \mathbb{R}^p$ is defined as

$$z_k(\hat{\theta}) = y_k - \phi_k \hat{\theta}. \tag{3}$$

The vector $\hat{\theta} \in \mathbb{R}^{[\hat{n}p(m+p)]}$ of coefficients to be estimated is

$$\hat{\theta} \triangleq \mathrm{vec}\begin{bmatrix} \hat{F}_1 & \cdots & \hat{F}_{\hat{n}} & \hat{G}_1 & \cdots & \hat{G}_{\hat{n}} \end{bmatrix} = \mathrm{vec}\begin{bmatrix} \hat{\theta}_{\hat{F}} & \hat{\theta}_{\hat{G}} \end{bmatrix},$$

where $\hat{\theta}_{\hat{F}}$ and $\hat{\theta}_{\hat{G}}$ are the estimates of the denominator and numerator coefficients, defined by

$$\hat{\theta}_{\hat{F}} \triangleq \operatorname{vec}\begin{bmatrix}\hat{F}_1 & \cdots & \hat{F}_{\hat{n}}\end{bmatrix}, \tag{4}$$

$$\hat{\theta}_{\hat{G}} \triangleq \operatorname{vec}\begin{bmatrix}\hat{G}_1 & \cdots & \hat{G}_{\hat{n}}\end{bmatrix}. \tag{5}$$

With the regressor matrix $\phi_k \in \mathbb{R}^{p\times[\hat{n}p(m+p)]}$ defined by

$$\phi_k \triangleq \begin{bmatrix}-y_{k-1}^{\mathrm{T}} & \cdots & -y_{k-\hat{n}}^{\mathrm{T}} & u_{k-1}^{\mathrm{T}} & \cdots & u_{k-\hat{n}}^{\mathrm{T}}\end{bmatrix} \otimes I_p,$$

the global minimizer $\theta_{k+1} \triangleq \operatorname{argmin}_{\hat{\theta}} J_k(\hat{\theta})$ of (2) is

$$L_k = \lambda_k^{-1} P_k, \tag{6}$$

$$P_{k+1} = L_k - L_k\phi_k^{\mathrm{T}}(I_p + \phi_k L_k \phi_k^{\mathrm{T}})^{-1}\phi_k L_k, \tag{7}$$

$$\theta_{k+1} = \theta_k + P_{k+1}\phi_k^{\mathrm{T}}(y_k - \phi_k\theta_k). \tag{8}$$

The variable-rate forgetting factor $\lambda_k$ is given by [6]

$$\lambda_k = \frac{1}{1 + \eta g(z_{k-\tau_{\mathrm{d}}}, \ldots, z_k)\mathbf{1}[g(z_{k-\tau_{\mathrm{d}}}, \ldots, z_k)]}, \tag{9}$$

where $\mathbf{1}\colon \mathbb{R} \to \{0, 1\}$ is the unit step function, and

$$g(z_{k-\tau_{\mathrm{d}}}, \ldots, z_k) \triangleq \sqrt{\frac{\tau_{\mathrm{n}}}{\tau_{\mathrm{d}}}\frac{\left(\Sigma_{\tau_{\mathrm{n}}}(z_{k-\tau_{\mathrm{n}}}, \ldots, z_k)\Sigma_{\tau_{\mathrm{d}}}(z_{k-\tau_{\mathrm{d}}}, \ldots, z_k)^{-1}\right)}{c}} - \sqrt{f},$$

where $\eta > 0$ and $p \le \tau_{\mathrm{n}} < \tau_{\mathrm{d}}$ represent numerator and denominator window lengths. $\Sigma_{\tau_{\mathrm{n}}}$ and $\Sigma_{\tau_{\mathrm{d}}}$ are the sample variances of the respective window lengths, and the threshold constant $f$ is described in [6, 25]. The constant $c$, based on the windows lengths is described in [6]. The estimator coefficients $\hat{\theta}$ can be written in the block observable canonical form with matrices $\hat{A}_k$, $\hat{B}_k$, and $\hat{C}_k$ given by

$$\hat{A}_k \triangleq \begin{bmatrix}-\hat{F}_{1,k} & I_p & \cdots & \cdots & 0_{p\times p}\\ \vdots & 0_{p\times p} & \ddots & & \vdots\\ \vdots & \vdots & \ddots & \ddots & 0_{p\times p}\\ \vdots & \vdots & & \ddots & I_p\\ -\hat{F}_{\hat{n},k} & 0_{p\times p} & \cdots & \cdots & 0_{p\times p}\end{bmatrix}, \quad \hat{B}_k \triangleq \begin{bmatrix}\hat{G}_{1,k}\\ \hat{G}_{2,k}\\ \vdots\\ \hat{G}_{\hat{n},k}\end{bmatrix}, \tag{10}$$

$$\hat{C}_k \triangleq \begin{bmatrix}I_p & 0_{p\times p} & \cdots & 0_{p\times p}\end{bmatrix}. \tag{11}$$

**B. Model Predictive Control**

Model predictive control (MPC) uses a model of the system to optimize the future performance over a time horizon. The optimization yields a sequence of controls, the first of which is implemented, and the procedure is repeated at subsequent steps. By performing constrained optimization, MPC enforces constraints on the control input and plant outputs [26–29]. At step $k$, PCAC uses the identified model $\hat{A}_k$, $\hat{B}_k$, and $\hat{C}_k$. As in [1], receding-horizon optimization is performed using quadratic programming (QP), which is a convex optimization technique. This optimization determines the control input $u_{k+1}$ at the next time step, while also attempting to satisfy constraints on the state and control input

To describe QP-based MPC, let $\mathcal{R}_{k,\ell} \triangleq \begin{bmatrix}r_{k+1}^{\mathrm{T}} \cdots r_{k+\ell}^{\mathrm{T}}\end{bmatrix}^{\mathrm{T}} \in \mathbb{R}^{\ell p_{\mathrm{t}}}$ be the vector of future commands over the horizon $\ell$, let $Y_{1|k,l}$ be the corresponding $l$-step predicted output for a sequence of $l$ future controls, $U_{1|k,l}$, and let $Y_{\mathrm{t},1|k,\ell} \triangleq C_{\mathrm{t},\ell}Y_{1|k,\ell}$ be the $\ell$-step predicted output, where $C_{\mathrm{t},\ell} \triangleq I_\ell \otimes C_{\mathrm{t}} \in \mathbb{R}^{\ell p_{\mathrm{t}}\times\ell p}$, $\otimes$ is the Kronecker product, and

$C_{\mathrm{t}} y_{i|k}$ computes the tracking outputs from $y_{i|k}$. Let $C_\ell \triangleq I_\ell \otimes (C C_{\mathrm{c}}) \in \mathbb{R}^{\ell n_{\mathrm{c}} \times \ell p}$, where $C_{\mathrm{c}} y_{i|k}$ creates the constrained outputs from $y_{i|k}$, let $\mathcal{D}_\ell \triangleq 1_\ell \otimes \mathcal{D} \in \mathbb{R}^{\ell n_{\mathrm{c}}}$, and define the sequence of differences of control inputs as

$$\Delta U_{1|k,\ell} \triangleq \begin{bmatrix} (u_{1|k} - u_k)^{\mathrm{T}} & \cdots & (u_{\ell|k} - u_{\ell-1|k})^{\mathrm{T}} \end{bmatrix}^{\mathrm{T}} \in \mathbb{R}^{\ell m}. \tag{12}$$

The QP-based MPC optimization problem is then given by

$$\min_{U_{1|k,\ell}} \left(Y_{\mathrm{t},1|k,\ell} - \mathcal{R}_{k,\ell}\right)^{\mathrm{T}} Q \left(Y_{\mathrm{t},1|k,\ell} - \mathcal{R}_{k,\ell}\right) + \Delta U_{1|k,\ell}^{\mathrm{T}} R \Delta U_{1|k,\ell}, \tag{13}$$

subject to

$$C_\ell Y_{1|k,\ell} + \mathcal{D}_\ell \le 0_{\ell n_{\mathrm{c}}}, \tag{14}$$

$$U_{\min} \le U_{1|k,\ell} \le U_{\max}, \tag{15}$$

$$\Delta U_{\min} \le \Delta U_{1|k,\ell} \le \Delta U_{\max}, \tag{16}$$

where $Q \triangleq \begin{bmatrix} \bar{Q} & 0_{(\ell-1)p_{\mathrm{t}} \times p_{\mathrm{t}}} \\ 0_{p_{\mathrm{t}} \times (\ell-1)p_{\mathrm{t}}} & \bar{P} \end{bmatrix} \in \mathbb{R}^{\ell p_{\mathrm{t}} \times \ell p_{\mathrm{t}}}$ is the output weighting, $\bar{Q} \in \mathbb{R}^{(\ell-1)p_{\mathrm{t}} \times (\ell-1)p_{\mathrm{t}}}$ is the cost-to-go output weighting, $\bar{P} \in \mathbb{R}^{p_{\mathrm{t}} \times p_{\mathrm{t}}}$ is the terminal output weighting, $R \in \mathbb{R}^{\ell m \times \ell m}$ is the control-move-size weighting, $U_{\min} \triangleq 1_\ell \otimes u_{\min} \in \mathbb{R}^{\ell m}$, $U_{\max} \triangleq 1_\ell \otimes u_{\max} \in \mathbb{R}^{\ell m}$, $\Delta U_{\min} \triangleq 1_\ell \otimes \Delta u_{\min} \in \mathbb{R}^{\ell m}$, and $\Delta U_{\max} \triangleq 1_\ell \otimes \Delta u_{\max} \in \mathbb{R}^{\ell m}$.

## III. Simulation Setup

All examples in this paper were computed using either ANSYS Fluent or xflow. Fluent is interfaced with the MATLAB-based PCAC control code using a custom Fluent user-defined function (UDF) employing the MATLAB Engine API. xflow is interfaced with PCAC using the MATLAB Engine API directly. In both cases, at each controller timestep $k$, the interface obtains measurements $y_k$ from the flow field, and provides it to PCAC. PCAC uses $y_k$ to compute the performance variable $z_k$, which it uses to compute the control inputs $u_k$ The interface then sends $u_k$ to the CFD solver, which applies the control input by modifying the associated actuator boundary conditions or by modifying the mesh geometry. This paper considers an airfoil placed above a periodic traveling wave. The wave motion is prescribed to model an airfoil flying over a static, wavy surface at a specified ground speed.

## IV. Application of PCAC to Ground Effect Flight with Control Jet

In the following examples, we use ANSYS Fluent and consider the NACA 4414 airfoil at 10-deg angle of attack with 1 m chord. This airfoil is placed 1 m above the wavy surface with amplitude of 0.5 m and and wavelength of 3 m. We assume an idealized estimate of airfoil lift $y_k$ at each timestep. PCAC uses the estimate to compute the performance variable $z_k$. PCAC specifies the velocity $u_k$ of a control jet placed at the lower surface of the airfoil trailing edge and oriented downwards toward the wavy surface. This jet can force air in either direction, with a negative sign indicating flow into the airfoil. The wave motion induces a disturbance in the lift, approximately periodic with frequency dependent on the traveling wave speed. The control goal is to use only the idealized lift estimate to actuate the jet in order to reject the disturbance in airfoil lift.

Figure 2 shows the mesh, which extends for approximately 9 chords in front, behind, and above the airfoil. The control jet is represented by a velocity inlet boundary condition, with the velocity being specified at each time step by PCAC. The airfoil surface is represented with a no-slip wall. The wave surface is represented with a zero-sheer wall. The wave motion is defined such that each cell bounding the wave moves vertically in a phase such the the wave travels downstream at a velocity equal to the prescribed airfoil ground speed. However, because the mesh cells themselves do not translate downstream, the flow must be allowed to slip along the wall boundary, otherwise, a non-physical boundary layer would form on the wave surface.

**Example 1.** *IGE Flight under Constant Conditions.* In this example, we consider steady flight (constant speed, altitude, and pitch) without additional disturbances. Here, PCAC operates with a lift setpoint that is approximately the average of the uncontrolled oscillating lift. The control objective is to reduce the magnitude of the lift oscillations

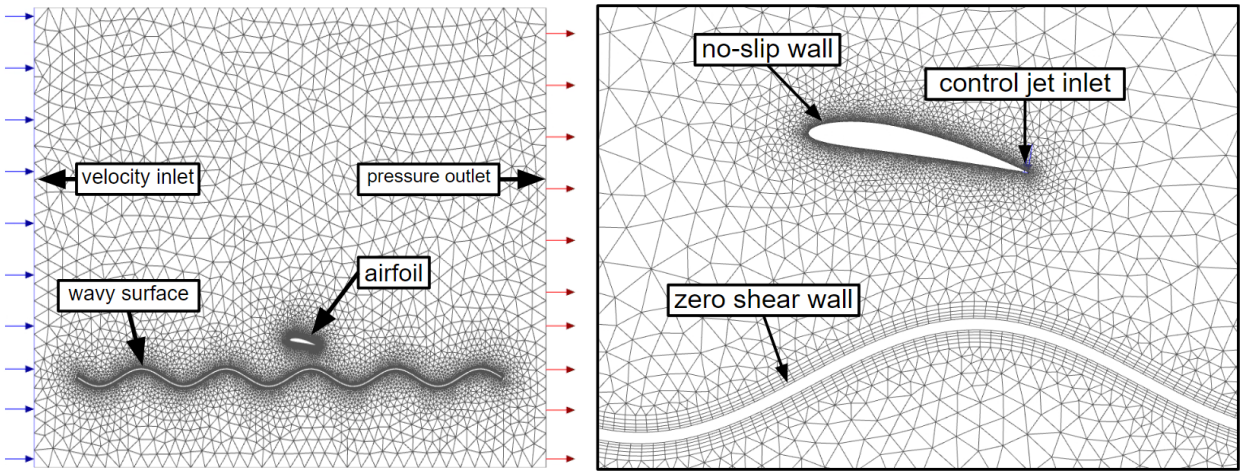


**Fig. 2 Full Fluent case mesh (left) and mesh zoomed to airfoil region (right).**

without using the jet to apply a bias to the generated lift. The wave speed and freestream velocity are synced at 50 m/s. This induces an apparent wave frequency of 16.667 Hz at the airfoil and an associated disturbance in lift near the same frequency. Figure 3 shows the sensor measurements, requested control input, model coefficients estimated by RLSID, and RLS forgetting factor. A clear disturbance is present in the airfoil lift before the controller is enabled at 0.3 s. Within 0.2 s, the magnitude of this disturbance is reduced by PCAC. Figure 4 shows the measurements and spectrum of the lift for the controlled and uncontrolled case, with a peak in the spectrum at the apparent wave frequency.

◇

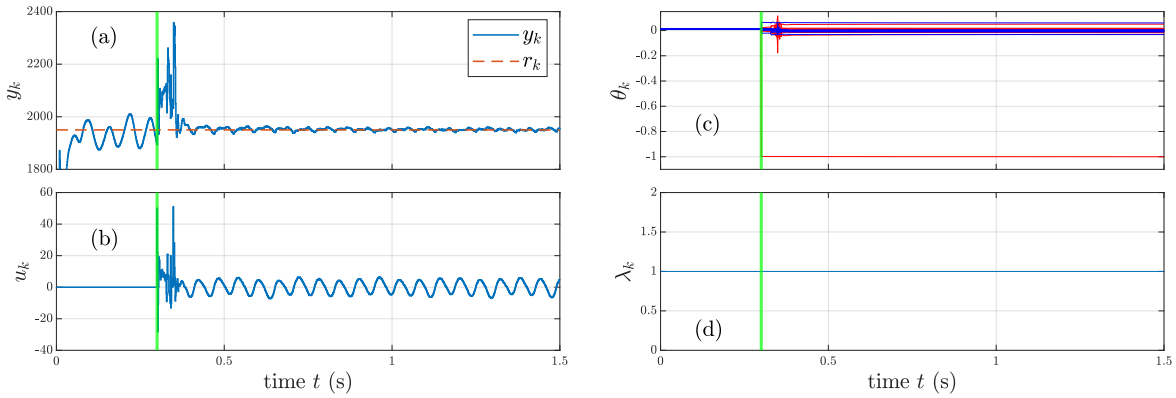


**Fig. 3 Example 1: (a) shows that the oscillations in the lift are reduced following a transient when the controller is enabled (green line). (b) shows the PCAC-commanded control-jet velocities. (c) shows the time histories of the numerator (blue) and denominator (red) coefficients of the identified model. (d) shows the variable-rate forgetting factor, which is inactive in this scenario.**

**Example 2.** *IGE Flight with Constant Headwind.* Reconsider Example 1 with the freestream velocity increased to 60 m/s while maintaining the wave speed of 50 m/s, representing the airfoil flying with 50-m/s ground speed and a 10-m/s headwind. The commanded lift is increased to the new average uncontrolled lift. All controller hyperparameters remain identical to those used in Example 1.

Figure 5 shows the sensor measurements, requested control input, model coefficients estimated by RLSID, and RLS forgetting factor. A clear disturbance is present in the airfoil lift before the controller is enabled at 0.3 s. Within 0.2 s, the magnitude of this disturbance is reduced by PCAC.

◇

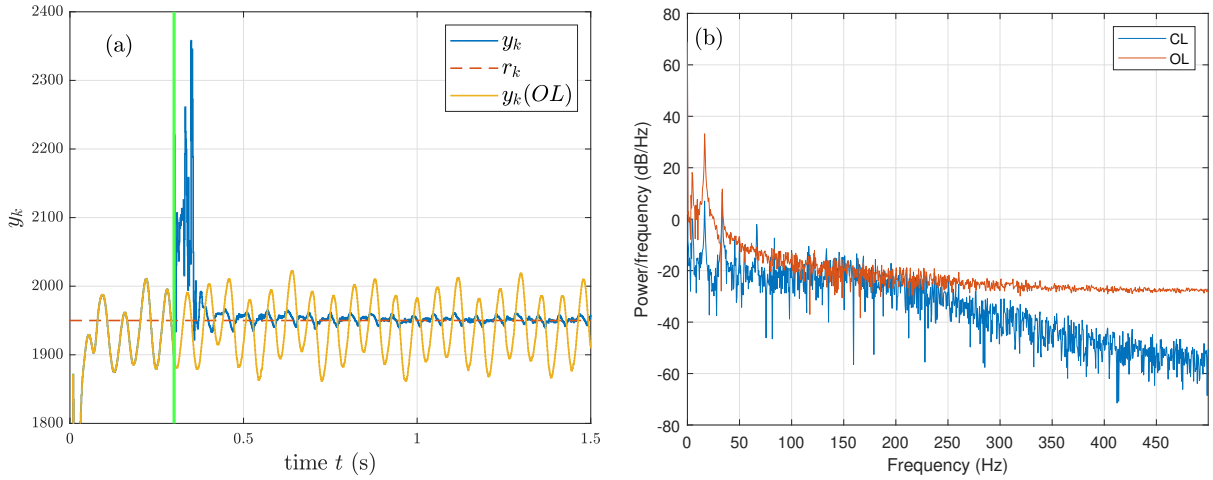


**Fig. 4 Example 1: Open- and closed-loop lift measurements (a) and PSD of the lift estimates in the controlled and uncontrolled cases (b). A peak is present near the disturbance frequency of 16.667 Hz. At this frequency, the controller achieves approximately 26 dB suppression over the last 1000 samples. This suppression is at the cost of spillover between 100 and 200 Hz, consistent with the Bode integral constraint.**

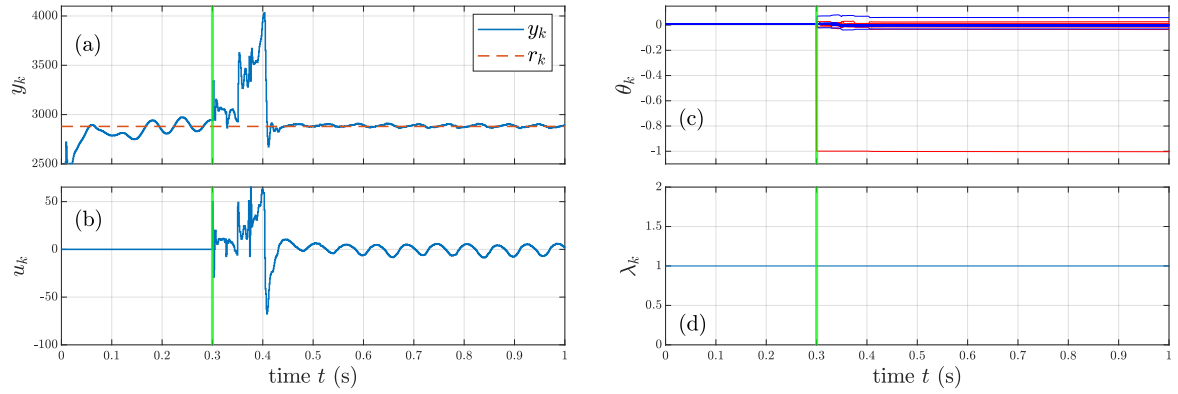


**Fig. 5 Example 2: (a) shows that the oscillations in the lift are reduced following a transient when the controller is enabled (green line). (b) shows the PCAC-commanded control-jet velocities. (c) shows the time histories of the numerator (blue) and denominator (red) coefficients of the identified model. (d) shows the variable-rate forgetting factor which is inactive in this scenario.**

**Example 3.** *IGE Flight under Acceleration.* Reconsider Example 1 with the airfoil undergoing acceleration in-ground-effect flight between two phases of constant-speed flight. In this example, the airfoil accelerates from 50 m/s to 60 m/s in 1 s. No wind is assumed, so the freestream velocity and wave speed both increase in sync. In each of the constant-speed phases, the commanded lift is approximately the average of the uncontrolled lift. In the acceleration phase, the commanded lift increases linearly between the commands of the constant speed phases. Figure 6 shows the sensor measurements, requested control input, model coefficients estimated by RLSID, and RLS forgetting factor. A clear disturbance is present in the airfoil lift before the controller is enabled at 0.3 s. Within 0.2 s, the magnitude of this disturbance is reduced by PCAC. Figure 7 shows a comparison of the lift between the controlled and uncontrolled case. Figure 8 shows the spectrum of the lift for the controlled and uncontrolled cases during each constant speed phase. In each phase, a peak in the frequency response is visible near apparent wave frequency.

◇

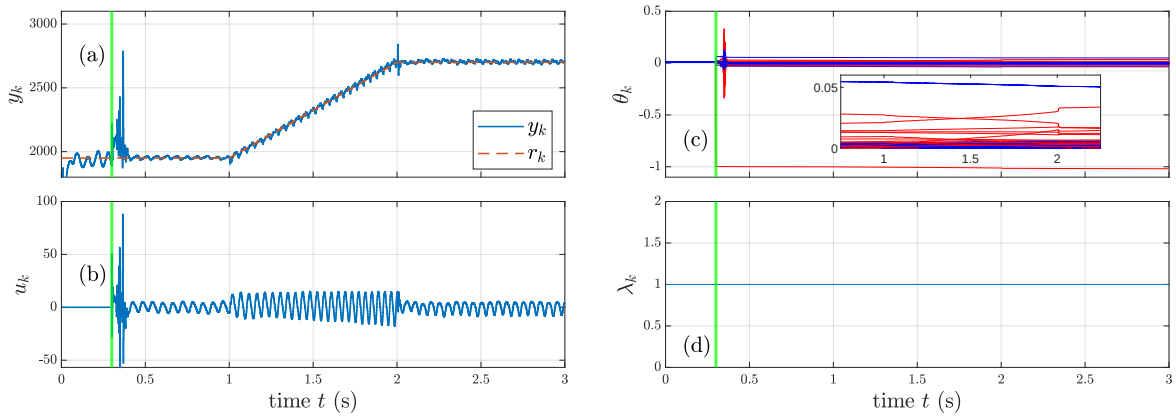


**Fig. 6 Example 3: (a) shows that the oscillations in the lift are reduced following a transient when the controller is enabled (green line). (b) shows the PCAC commanded control jet velocities. (c) shows the time histories of the numerator (blue) and denominator (red) coefficients of the identified model, where the inset plot shows the identified model adapting as the airfoil accelerates. (d) shows the variable-rate forgetting factor which is inactive in this scenario.**

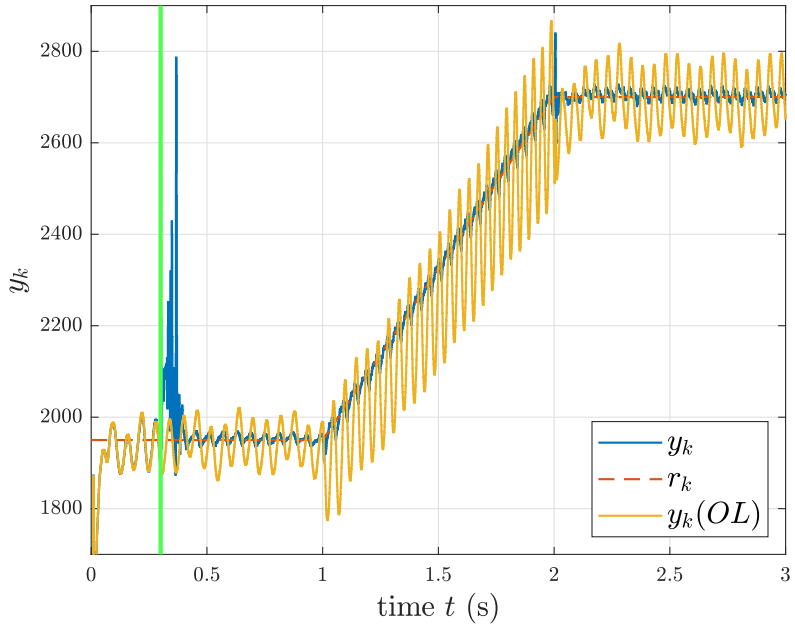


**Fig. 7 Example 3: Open vs Closed loop lift measurements. The lift oscillation is suppressed in both constant-speed phases and the acceleration phase.**

## V. Application of PCAC to Ground Effect Flight with Flap Actuator

We also consider an alternate actuation, a trailing-edge flap, to suppress oscillations in the lift. For this case, the simulations are done using xflow, a high-order discontinuous Galerkin finite-element code [30]. The airfoil is a NACA 0012 flying in subsonic conditions, $M = 0.5$. The governing equations are compressible Euler, and both the moving wall and the flap actuation are simulated using an arbitrary Lagrangian-Eulerian mesh motion capability [31, 32]. The units for this problem are convenient $O(1)$ quantities in which one time unit corresponds to the time taken by flow moving at freestream speed to traverse the airfoil chord. For convenience, we call this time unit seconds.

Figure 9 shows the computational mesh, which is unstructured and generated using metric-based mesh optimization [33] under the conditions of steady-state, flat-ground, and zero-flap deflection. With the moving ground, the lift

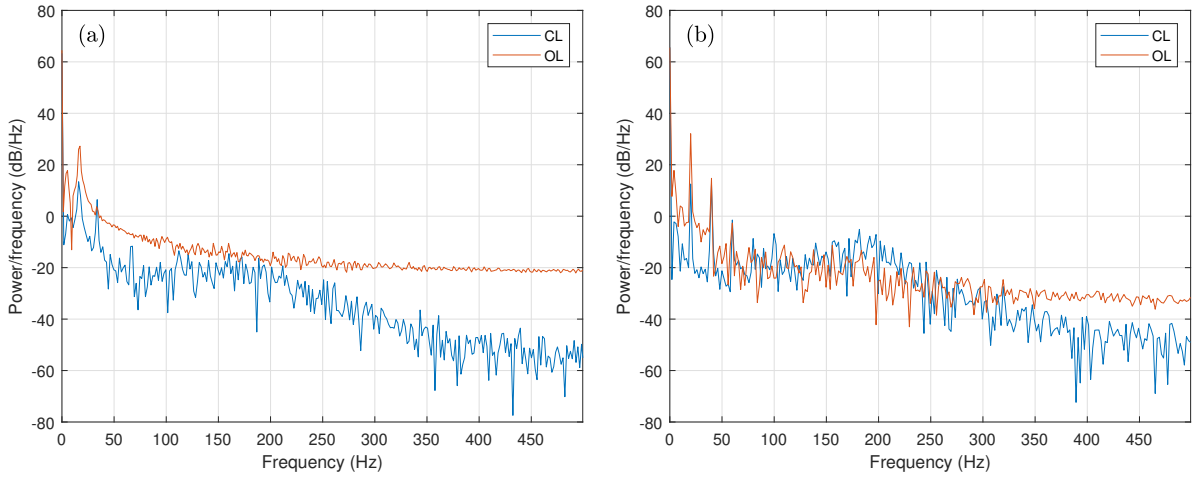


**Fig. 8 Example 3: PSD of the lift estimates in 50 m/s phase (a) and 60 m/s phase (b). In both plots, a peak is present near the apparent wave frequencies of 16.667 Hz and 20 Hz respectively. At 50 m/s, the controller achieves a suppression of approximately 14 dB over the last 500 samples before acceleration. At 60 m/s, the controller achieves a suppression of approximately 20 dB over the last 500 samples.**

coefficient exhibits oscillatory behavior.

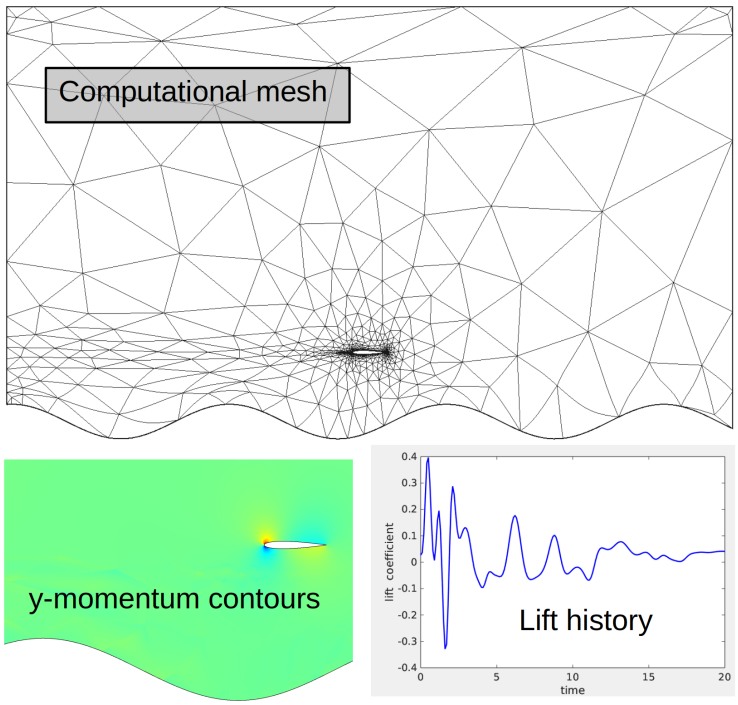


**Fig. 9 Flap actuator test case setup in xflow, showing the computational mesh, solution snapshot, and lift coefficient time history.**

**Example 4.** *IGE Flight under Constant Conditions*. In this example we consider again the case of steady flight without additional disturbances. The oscillatory behavior of the lift coefficient is made more clear in Figure 10, which shows the open-loop results before the controller is turned on. The oscillations in the lift are due to the proximity of the lower boundary, which consists of a travelling sinusoidal wave. When PCAC is turned on at 0 s, the flap deflection

exhibits seemingly oscillatory behavior as PCAC begins to learn the system dynamics. At this time, the lift coefficient continues to oscillate, with additional higher harmonics and aperiodic behavior. Around 40 s, the controller settles in on a periodic flap deflection that damps out the lift oscillations. After this time, although the lift is not completely constant, the oscillations are minor compared to the open-loop case. Figure 10 also shows the model parameters and forgetting factor. We see an initial slow change in the model parameters until the forgetting becomes active, at which point the model parameters oscillate wildly. Following the oscillations, the parameters converge to steady-state values at approximately the same time that the lift oscillations are suppressed.

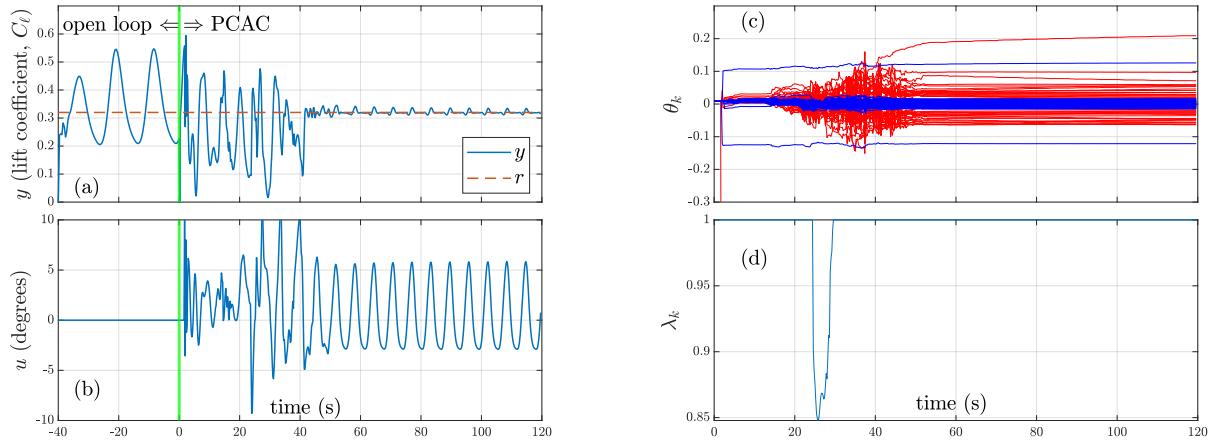


**Fig. 10 Example 4: (a) shows that the oscillations in the lift are reduced following a transient when the controller is enabled. (b) shows the PCAC commanded control jet velocities which oscillate. (c) shows the time histories of the numerator (blue) and denominator (red) coefficients. (d) shows the variable-rate forgetting factor, which is active between 25 and 30 s where $\lambda_k < 1$.s**

## VI. Conclusions

This paper considered the ability of PCAC to suppress oscillations in lift due to in-ground-effect flight over a wavy surface. The paper considered the cases of steady flight, steady flight with a headwind, and accelerating flight. The paper also considered control-jet actuation and flap actuation. In all cases, PCAC suppressed oscillations without the need for either analytical modeling or data-intensive offline training. This ability shows that PCAC is potentially effective for IGE flight in complex, realistic situations.

## VII. Acknowledgments

This research was supported by ONR grants N00014-22-1-2457 and N00014-24-1-2285.

## References

[1] Nguyen, T. W., Islam, S. A. U., Bernstein, D. S., and Kolmanovsky, I. V., "Predictive Cost Adaptive Control: A Numerical Investigation of Persistency, Consistency, and Exigency," *IEEE Contr. Sys. Mag.*, Vol. 41, 2021, pp. 64–96.

[2] Islam, S. A. U., and Bernstein, D. S., "Recursive Least Squares for Real-Time Implementation," *IEEE Contr. Syst. Mag.*, Vol. 39, No. 3, 2019, pp. 82–85.

[3] Bruce, A. L., Goel, A., and Bernstein, D. S., "Convergence and consistency of recursive least squares with variable-rate forgetting," *Automatica*, Vol. 119, 2020, p. 109052.

[4] Goel, A., Bruce, A. L., and Bernstein, D. S., "Recursive Least Squares With Variable-Direction Forgetting: Compensating for the Loss of Persistency [Lecture Notes]," *IEEE Control Systems Magazine*, Vol. 40, No. 4, 2020, pp. 80–102.

[5] Bruce, A. L., Goel, A., and Bernstein, D. S., "Necessary and Sufficient Regressor Conditions for the Global Asymptotic Stability of Recursive Least Squares," *Sys. Contr. Lett.*, Vol. 157, 2021, pp. 1–7. Article 105005.

[6] Mohseni, N., and Bernstein, D. S., "Recursive least squares with variable-rate forgetting based on the F-test," *Proc. Amer. Contr. Conf.*, 2022, pp. 3937–3942.

[7] Polderman, J. W., "A State Space Approach to the Problem of Adaptive Pole Assignment," *Mathematics of Control, Signals and Systems*, Vol. 2, No. 1, 1989, pp. 71–94.

[8] Bewley, T. R., "Flow control: new challenges for a new renaissance," *Progress in Aerospace sciences*, Vol. 37, No. 1, 2001, pp. 21–58.

[9] Aamo, O. M., and Krstic, M., *Flow Control by Beedback: Stabilization and Mixing*, Springer, 2003.

[10] Gunzburger, M. D., *Perspectives in Flow Control and Optimization*, SIAM, 2002.

[11] Gad-el Hak, M., *Flow Control: Passive, Active, and Reactive Flow Management*, Cambridge University Press, 2000.

[12] Joslin, R. D., and Miller, D. N. (eds.), *Fundamentals and Applications of Modern Flow Control*, AIAA, 2009.

[13] Barbu, V., *Stabilization of Navier–Stokes Flows*, Springer, 2011.

[14] Cattafesta III, L. N., and Sheplak, M., "Actuators for active flow control," *Ann. Rev. Fluid Mech.*, Vol. 43, 2011, pp. 247–272.

[15] Luhar, M., Sharma, A. S., and McKeon, B. J., "Opposition control within the resolvent analysis framework," *J. Fluid Mech.*, Vol. 749, 2014, p. 597–626.

[16] Brunton, S. L., and Noack, B. R., "Closed-loop turbulence control: Progress and challenges," *Appl. Mech. Rev.*, Vol. 67, No. 5, 2015.

[17] Duriez, T., Brunton, S. L., and Noack, B. R., *Machine Learning Control—Taming Nonlinear Dynamics and Turbulence*, Springer, 2017.

[18] Wang, J., and Feng, L., *Flow Control Techniques and Applications*, Cambridge University Press, 2019.

[19] Joshi, S. S., Speyer, J. L., and Kim, J., "A Systems Theory Approach to the Feedback Stabilization of Infinitesimal and Finite-Amplitude Disturbances in Plane Poiseuille Flow," *J. Fluid Mech.*, Vol. 332, 1997, pp. 157–184.

[20] Joshi, S. S., Speyer, J. L., and Kim, J., "Finite Dimensional Optimal Control of Poiseuille Flow," *J. Guid. Contr. Dyn.*, Vol. 22, 1999, pp. 340–348.

[21] Bewley, T. R., and Liu, S., "Optimal and robust control and estimation of linear paths to transition," *J. Fluid Mech.*, Vol. 365, 2001, pp. 305–349.

[22] Gautier, N., Aider, J.-L., Duriez, T., Noack, B., Segond, M., and Abel, M., "Closed-loop separation control using machine learning," *J. Fluid Mech.*, Vol. 770, No. 5, 2015, pp. 442–457.

[23] Wang, Z., Fidkowski, K., Abgrall, R., Bassi, F., Caraeni, D., Cary, A., Deconinck, H., Hartmann, R., Hillewaert, K., Huynh, H., Kroll, N., May, G., Persson, P.-O., van Leer, B., and Visbal, M., "High-Order CFD Methods: Current Status and Perspective," *International Journal for Numerical Methods in Fluids*, Vol. 72, 2013, pp. 811–845. https://doi.org/10.1002/fld.3767.

[24] Fidkowski, K. J., and Darmofal, D. L., "Review of Output-Based Error Estimation and Mesh Adaptation in Computational Fluid Dynamics," *AIAA Journal*, Vol. 49, No. 4, 2011, pp. 673–694. https://doi.org/10.2514/1.J050073.

[25] McKeon, J. J., "F approximations to the distribution of Hotelling's $T_0^2$," *Biometrika*, Vol. 61, No. 2, 1974, pp. 381–383.

[26] Kwon, W., and Han, S., *Receding Horizon Control: Model Predictive Control for State Models*, Springer, 2006.

[27] Rawlings, J. B., Mayne, D. Q., and Diehl, M. M., *Model Predictive Control: Theory, Computation, and Design*, Nob Hill, 2020.

[28] Tao, J., Ma, L., and Zhu, Y., "Improved control using extended non-minimal state space MPC and modified LQR for a kind of nonlinear systems," *ISA Trans.*, Vol. 65, 2016, pp. 319–326.

[29] Eren, U., Prach, A., Koçer, B. B., Raković, S. V., Kayacan, E., and Açıkmeşe, B., "Model predictive control in aerospace systems: Current state and opportunities," *J. Guid. Contr. Dyn.*, Vol. 40, No. 7, 2017, pp. 1541–1566. https://doi.org/10.2514/1.G002507.

[30] Fidkowski, K. J., "Output error estimation strategies for discontinuous Galerkin discretizations of unsteady convection-dominated flows," *International Journal for Numerical Methods in Engineering*, Vol. 88, No. 12, 2011, pp. 1297–1322. https://doi.org/10.1002/nme.3224.

[31] Persson, P.-O., Bonet, J., and Peraire, J., "Discontinuous Galerkin Solution of the Navier-Stokes Equations on Deformable Domains," *Computer Methods in Applied Mechanics and Engineering*, Vol. 198, 2009, pp. 1585–1595.

[32] Kast, S. M., and Fidkowski, K. J., "Output-based Mesh Adaptation for High Order Navier-Stokes Simulations on Deformable Domains," *Journal of Computational Physics*, Vol. 252, No. 1, 2013, pp. 468–494. https://doi.org/10.1016/j.jcp.2013.06.007.

[33] Fidkowski, K. J., "A Local Sampling Approach to Anisotropic Metric-Based Mesh Optimization," AIAA Paper 2016–0835, 2016. https://doi.org/10.2514/6.2016-0835.